The influence of a KCl-rich environment on the corrosion attack of 304 L: 3D FIB/SEM and TEM investigations

Corrosion Science 183 (2021) 109315

Contents lists available at ScienceDirect

Corrosion Science

journal homepage: www.elsevier.com/locate/corsci

The influence of a KCl-rich environment on the corrosion attack of 304 L: 3D FIB/SEM and TEM investigations

J. Phother-Simon, I. Hanif *, J. Liske, T. Jonsson

Environmental Inorganic Chemistry, Department of Chemistry and Chemical Engineering, Chalmers University of Technology, SE-412 96, Göteborg, Sweden

ARTICLE INFO

Keywords:
Intergranular corrosion
304L
TEM
High-temperature corrosion
3D tomography

ABSTRACT

This study investigates the intergranular corrosion of a stainless steel (304 L) in the presence of KCl(g)/KCl(s) at 600 °C by using a FIB/SEM to perform 3D reconstruction/tomography of grain boundary attacks in combination with TEM. The investigation shows that the combination of the 3D FIB/TEM offers a great potential for the study of complex features, i.e. intergranular corrosion. The initiation and propagation of the grain boundary attack occurred very rapidly below an intact secondary protection. No large accumulations of metal chlorides were observed at the grain boundary regions. Instead, indications of very rapid alloy diffusion in grain boundary regions were observed.

1. Introduction

In order to reduce the net emission of carbon dioxide (CO_2), power plants have been gradually increasing the fraction of renewable fuels as a substitute for fossil fuels [1]. However, the combustion of these renewable fuels such as biomass and waste, can cause the formation of corrosive deposits and gases that deteriorate essential parts of the plant such as superheaters. The combustion of biomass and waste results in a flue gas containing mainly water vapor, carbon dioxide, alkali chlorides and hydrogen chloride [2–8]. Alkali chlorides are well-known for their corrosiveness towards superheater tubes [2,7,9–19].

The corrosiveness of alkali chlorides has been explained by the "chromate formation" mechanism [2,7,9–21], which involves the alkali to break down the protective chromium-rich scale of stainless steels via the formation of alkali chromate resulting in iron-rich non-protective scale. This would explain the initiation and the frequent observation of a missing chromia scale on stainless steels in these environments. An alternative mechanism is the so-called "active oxidation" mechanism [7, 11,22–27], which relies on the transport of $Cl_2(g)$ through the oxide scale to the oxide/metal interface. The $Cl_2(g)$ then reacts with the metal to form metal chlorides that diffuse as $MeCl_x(g)$ back through the oxide scale, cracks and pores, towards the gas/oxide interface. The higher partial pressure of oxygen at the gas/oxide interface leads to the decomposition of the metal chlorides $MeCl_x(g)$ into the metal oxide Me_xO_y, releasing $Cl_2(g)$ to the atmosphere. The released $Cl_2(g)$ can be transported again towards the metal/oxide interface, repeating the process in a cyclic manner. "Active oxidation" or the chlorine cycle is a well-known suggested mechanism that describes chlorine-induced corrosion. However, the approach remains theoretical, and several aspects of the suggested mechanism exhibit debatable elements. Assuming that $Cl_2(g)$ can penetrate through the oxide scale and reach the metal/oxide interface, then the oxygen molecule $O_2(g)$ would be able to penetrate the oxide scale as well, as its size (~292 pm) is smaller than $Cl_2(g)$ (~396 pm). The possibility for the oxygen molecule to travel through the oxide scale and reach the metal/oxide interface would decrease the probability of metal chlorides forming as the gradient of oxygen partial pressure through the oxide scale would change. The "active oxidation" mechanism also suggests that the formation of metal chlorides occurs at the metal/oxide interface, while the presence of metal chlorides on the outer part of the oxide scale has been reported as well [23,27]. For these reasons, the so-called electrochemical approach has been elaborated. The mechanism suggests a flux of anions, cations, and electronic current as a diffusion mechanism, instead of a gas transport of chlorine through the oxide scale [23,28,29].

It was recently shown that adding KCl from the gas phase may lead to accelerated corrosion of a 304 L-type stainless steel [30]. The microstructure was reported to consist of outward- and inward-growing oxides paired with a deep steel grain boundary (GB) attack. This type of microstructure is observed in studies in more complex environments, i.e. biomass-/waste-fired boilers [2,31]. However, the mechanism driving the intergranular corrosion is not known. One reason is that traditional microscopy-based investigations of the complex 3D microstructure of

* Corresponding author.
E-mail address: imran.hanif@chalmers.se (I. Hanif).

https://doi.org/10.1016/j.corsci.2021.109315
Received 3 November 2020; Received in revised form 20 January 2021; Accepted 6 February 2021
Available online 9 February 2021

intergranular corrosion are usually performed using techniques such as Scanning Transmission Electron Microscopy (STEM), Scanning Electron Microscope (SEM), and Energy Dispersive X-ray spectroscopy (EDX). These techniques are efficient for analyzing the chemistry and material information from the micro to nano scale. However, the two-dimensional aspect of these investigations makes it difficult to systematically investigate the corrosion front of a GB attack.

This study aims at increasing the understanding of the GB attack by providing more accurate representations of and new insights into intergranular corrosion in stainless steels by using a FIB/SEM to perform 3D reconstruction/tomography of GB attacks linked to a TEM characterization.

The investigation is focused on the commercially available 304 L stainless steel, exposed to a 5% O_2 + 20 % H_2O + N_2 bal. environment under continuous KCl deposition for 1-h and 24-h at 600 °C [30]. The experimental parameters were selected to simplify the flue gas composition released during biomass combustion in order to better understand the role of chlorine on the GB attack. The samples were exposed for 1-h and 24-h to characterize the initiation and growth (propagation) of the GB attack as well as the presence of chlorine in and around the grain boundaries to better understand the corrosion mechanisms and possibly, material degradation.

2. Materials and methods

2.1. Sample preparation

Austenitic steel 304 L was obtained from Outokumpu and the composition given in Table 1. The samples were cut and polished into the following dimensions: 15 × 15 × 2 mm with a hole of 1.5 mm diameter drilled at 2 and 7.5 mm from the edges. All samples were ground with 500 grit SiC from Struers and then polished with 9, 3, and 1 μm diamond solutions DP-Suspension using DP-Lubricant Yellow. As a final step, the samples were cleaned in acetone then ethanol using the Elmasonic P ultrasonic bathtub from Elma.

2.2. Exposures

The investigated samples were exposed to a 5% O_2 + 20% H_2O + N_2 (bal.) environment under continuous KCl deposition at 600 ℃. This was achieved by using a 3-zone furnace where an alumina boat filled with KCl(s) was placed upstream at 700 ℃ (calculated vapor pressure of KCl: 65.9 ppm) and the samples were placed downstream at 600 ℃ (calculated vapor pressure of KCl: 3.4 ppm). Thus, substantial deposition of KCl onto the samples occurred during the exposures. The position of the samples and the KCl boat were consistent for all exposures. The vapor pressures of KCl at the two temperatures were calculated using the software FactSage 7.2 [32] and the FTslat database. The duration of the exposures were 1-h and 24-h. A detailed description of the experimental setup is given in [30].

2.3. Broad Ion Beam (BIB)

Ion etching with Broad Ion Beam (BIB) milling was used to obtain cross-sections with smooth surfaces for SEM imaging. This technique uses a triple ion beam cutter Leica TIC 3X, which uses argon ions for milling. In order to prepare the sample for the BIB milling, a piece of silicon wafer was mounted on top of the sample surface using Loctite 415. After drying, the sample was cut into two pieces using the low-speed saw Minitom from Struers. One of the two pieces could be subsequently inserted in the BIB. The BIB machine was operated at 8.0 kV for 8 h.

Table 1
Chemical composition (wt. %) of 304 L.

Element (wt.%)	Fe	Cr	Ni	Mn	Si	P	S
304 L	Bal.	19.9	10	1.4	0.5	0.05	0.1

2.4. Scanning electron microscope and energy dispersive X-ray (SEM-EDX)

The SEM imaging was performed using a Quanta 200 ESEM FEG from FEI equipped with an Oxford Instruments X-Max^N 80 T EDX detector. The accelerating voltage used was 10 kV and 20 kV for imaging and EDX analysis, respectively. Both types of analyses were performed at a 10 mm working distance.

2.5. 3D tomography

3D tomography is a powerful SEM-based technique allowing more advanced characterization for a better understanding and interpretation of two-dimensional results. The technique has been mainly used in medical science [33–35] and is now emerging in the field of material science [36–45]. 3D tomography is currently being widely used in metallurgy and corrosion, allowing the characterization of very small features such as nanoscale precipitates, porosity in ceramics or cracks in oxide scales [36–45]. The geometry of such micro/nano scale features and their growth within the materials would not make this study possible by using the conventional two-dimensional techniques.

3D tomography is achieved by performing serial sectioning (slicing) to reconstruct areas of interest in 3D. This was carried out using a Tescan GAIA3 FIB/SEM system. Prior to sectioning, platinum was deposited onto the area of interest at 30 kV and a current of 2.3 nA. The sectioning was achieved at 10 nA (rough milling) and 7 nA (fine milling). Images were acquired with the integrated SEM using an accelerating voltage of 10 keV and SE detector. The images were then compiled as an image stack and processed in FIJI (Image J) software using the plugin StackReg with "Translation" as the transformation option [46–48]. The result of the image processing was a stack of well-aligned images in. tiff format.

3D Tomography was performed using the software Dragonfly version 4.1.0.647 [49]. The image stack was opened and processed directly within the software. The process, which aims at distinguishing different features of a dataset (image stack), is called segmentation. Several methods for segmentation exist [50,51] and in this study the method designated "thresholding" was used.

Thresholding is one of the simplest segmentation approache and is based on the pixel intensity values. The corrosion products observed in this experiment are well-known (such as voids or internal oxidation), while the range of intensity levels for thresholding was adapted to isolate the different features of interest. To avoid any faulty selection of **R**egions **O**f **I**nterest (ROI) by automatic segmentation due to similar intensity levels between pixels, a manual validation of the ROIs was conducted. This was achieved by using the ROI painter tool that allows accurate selection of ROIs for each slice (image). Once a feature of interest has been highlighted as a ROI in the dataset, it is possible to visualize several aspects of the ROI, such as spatial distribution, connectivity, or number of isolated elements. Three features of interest were converted to ROIs in this work: voids/cavities, nickel-rich nodules, and internal oxidation regions. The aims of using the 3D tomography technique were to obtain a better understanding of the void distribution in intergranular corrosion as well as to detect the of exact tips of GB attacks (corrosion front). The objective was to see if the tip of a GB attack (corrosion front) can be characterized by a specific morphology. This type of characterization cannot be achieved and interpreted by using only two-dimensional analyses. The 3D tomography technique will therefore provide detailed morphological (shape and depth) information of the GB attack. The observation of the void distribution and the exact tips of GB attacks was achieved by rendering the different ROIs into meshes. The meshes illustrated in Figs. 2, 7, and 8 were rendered in "solid" as filling mode and were smoothed using the Laplacian smoothing method with one iteration.

2.6. Transmission electron microscope (TEM) investigations

The 3D tomography analysis was linked to a detailed Transmission Electron Microscope (TEM) analysis. The TEM lamellas were prepared from BIB cross-sections using FEI Versa 3D FIB/SEM after interpreting the 3D structure with a 3D FIB. A protective platinum layer was deposited at 30 kV and a current of 0.3 nA. FIB trenches were made using 30 kV and the high current of 30 nA for rough milling. Cross-sections were fine milled using a current of 7 nA. After lifting out the sample with an Omniprobe needle and welding to a Cu TEM grid, the lamellas were thinned down with 30 kV at 1 nA. During the thinning down, the operating voltage and current was subsequently reduced until 8 kV and 30 pA, respectively. Lastly, thinned lamellas were plasma-cleaned using the Fischione 1020 Plasma Cleaner system at 2 kV for 5 min.

All TEM investigations were performed using an FEI Titan 80–300 equipped with an Oxford X-sight Energy Dispersive X-ray Spectroscopy (EDX) detector. The microscope was operated at 300 kV in Scanning TEM (STEM) mode under different conditions for microstructural investigations. For investigations, the FIB lamella was mounted in an FEI double tilt holder and was tilted to 15° so that it faced towards the EDX detector for acquisition. STEM-EDX was carried out to determine the chemical compositions of the features of interest using quantification, line scan, and elemental mapping. High Angle Annular Dark Field (HAADF) imaging was also employed in STEM mode. The TEM micrographs and EDX data was processed using an ImageJ and FEI's Tecnai Imaging and Analysis (TIA) software, respectively.

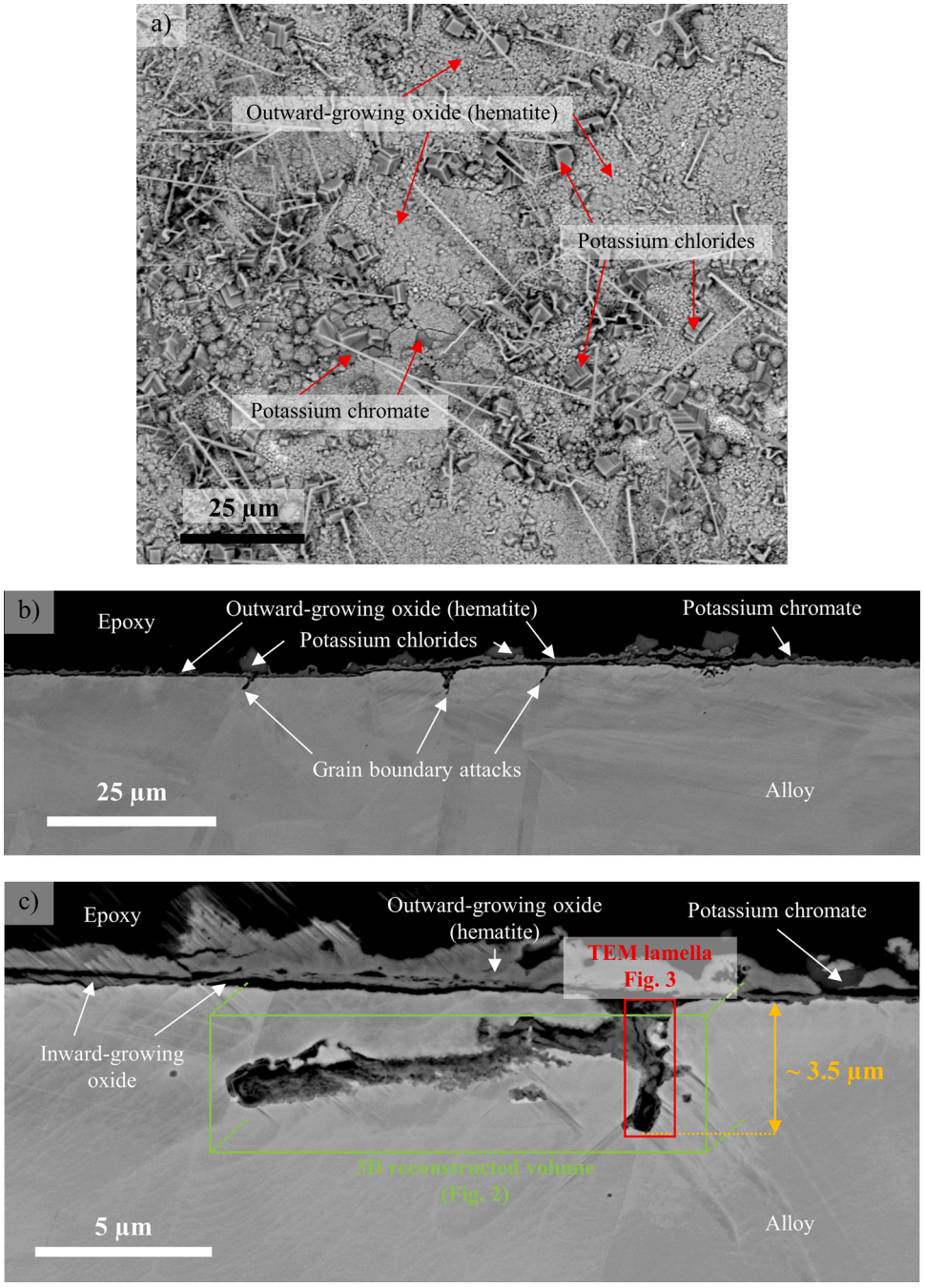

Fig. 1. BSE-SEM micrographs showing the plan view (a), low magnification (b) and high magnification (c) cross-sectional image of a 304 L sample exposed to 5% O_2 + 20 % H_2O + N_2 (bal.) under continuous KCl deposition at 600 °C for 1-h. The green and red rectangles in (c) refers to the area and volume investigated via 3D tomography (Fig. 2) (Fig. 3), respectively. The yellow arrow refers to the maximum depth of the GB attacks in this area. (For interpretation of the references to colour in the Figure, the reader is referred to the web version of this article).

3. Results

The focus of this work was on the initiation and the first step of the propagation of fast intergranular corrosion of the stainless steel 304 L in the presence of KCl. Samples exposed to a 5% O_2 + 20% H_2O + N_2 (bal.) environment under continuous KCl deposition for 1-h and 24-h at 600 °C were selected for the investigation. The objective was to investigate the initiation stage (1-h exposure) and the first step of propagation (24-h exposure) of the KCl-induced intergranular corrosion attack. For this reason, the results and discussion sections are divided into two subsections based on the duration of exposure.

Due to the experimental setup, heterogeneous deposition of KCl occurred on the sample surface [30]. Most of the deposition was observed on top of the standing samples (parallel to the gas flow) that stood in the furnace, while little deposition was found at the bottom of the sample. The top regions in addition exhibited a more severe corrosion attack (as well as intergranular corrosion) than the bottom parts. All characterizations were consequently performed in areas with large amounts of KCl deposits where the corrosion attack was more severe and intergranular corrosion was present.

3.1. 1-h exposure - Initiation

3.1.1. SEM analysis: plan view and cross-section

An optical inspection revealed some deposition of KCl(s) on the samples after one hour, which is in good agreement with an earlier morphology reported under similar conditions [30]. The SEM/BSE investigation showed that the salt was visible on top of an iron-rich oxide scale, and that potassium chromates and bright rods of iron oxide were present, see Fig. 1a. The iron oxide has been shown earlier to be outward-growing above an inward-growing FeCrNi oxide scale [12] and will therefore be referred as outward-growing in the interpretation of the results below.

After the plan view investigation, large crystals of KCl(s) were gently removed using an air duster in order to prepare ion-milled cross-sections of the corrosion products. The low magnification cross-section in Fig. 1b is in good agreement with the features observed in the plan view: a thin outward-growing oxide scale (iron oxide) with potassium chlorides and chromates on top of it. Below the iron oxide, a thin inward-growing FeCrNi oxide scale was observed. The initiation of GB attack can be seen in the BSE image, reaching a maximum depth of 3–4 µm at alloy grain boundaries below regions with a large amount of KCl deposited during exposure. Fig. 1c illustrates a typical region of GB attack at a higher magnification. The same corrosion products described previously can be seen with the addition of an observable inward-growing oxide scale. The average overall oxide thickness was ~ 0.9 µm with the outward-growing oxide being roughly 0.7 µm and the inward-growing oxide 0.2 µm. The GB attack reached a maximum depth of ~ 3.5 µm but could propagate laterally up to 10 µm and appeared to be typically characterized by voids and a fragile/brittle inward-growing oxide scale. This oxide also exhibits some porosity.

A large number of GB regions were characterized in several millimeters wide BIB cross-sections. Representative regions were selected from this investigation for the destructive 3D and TEM investigations. The marked region (green box) refers to the area and volume investigated via 3D tomography (see in Fig. 2). The marked red box labeled "TEM lamella" refers to a typical GB attack investigated via TEM (see Fig. 3). The yellow measurement annotation refers to the maximum depth of the GB attacks in this area.

3.1.2. 3D tomography analysis

3D tomography was used in order to investigate the grain boundary attacks.

The 3D results from a representative GB region (dominated by voids) are shown in Fig. 2. Very little corrosion products can be observed in the GB region. Instead, large voids dominate the microstructure after a 1-h exposure. This is in good agreement with the dark contrast observed using the BSE detector in the ion-milled cross-sections. The 3D technique can be utilized in order to determine if voids are interconnected in the investigated volume. The voids were therefore characterized into two categories, i.e. voids connected to the oxide/metal interface and isolated voids. The green mesh represents voids connected to the oxide/metal interface, while the red mesh represents voids not connected to the interface (isolated). A 2D SEM image using a BSE of the outward-growing oxide scale and the oxide/metal interface are displayed to make the illustration of the results easier to interpret. The results show that after one hour of exposure, approximatively 96% of the voids/cavities were connected to the surface, while the remaining 4% were isolated within the material (percentages calculated with Dragonfly). The voids are spread at and around alloy grain boundaries, but the representation does not cover all grain boundaries. The deepest GB attack of the investigated volume is represented by the yellow arrows and exhibits a tortuous microstructure. In addition, the voxel size of the 3D rendering was approximatively 50 nm, which implies that cavities smaller than this resolution could not be considered during the segmentation process and were therefore not rendered.

The 3D tomography also revealed indications of some corrosion products at the tips of GB attacks. However, the resolution of the SEM was too low to include these features in the 3D rendering, and TEM was used instead.

3.1.3. TEM analysis

A detailed TEM investigation was carried out to complement the 3D investigation and characterize the signs of corrosion products within and across the alloy grain boundaries. Thin TEM lamellas were made from selected positions on the BIB cross-sections after the 3D investigation was performed. The aim was to select representative regions containing the tips of GB attacks. Fig. 3a shows a STEM-HAADF image of a FIB lamella covering a representative GB attack after a one-hour exposure. The GB attack in this selected position reached a depth of approximately 3 µm beneath a 1.2 µm thick oxide scale. Using the 3D information, the discrete voids in the lamella are interpreted to be

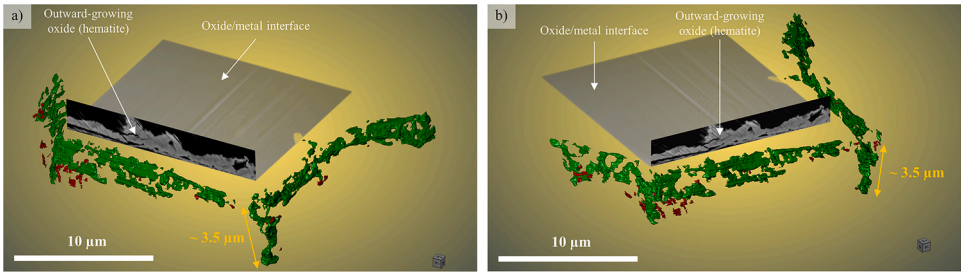

Fig. 2. a) 3D reconstruction of the voids from the area highlighted with green rectangle in Fig. 1c after 1-h of exposure and b) the same illustration from a different angle. The green mesh represents the voids connected to the oxide/metal interface. The red mesh represents the voids not connected to the surface. (For interpretation of the references to colour in the Figure, the reader is referred to the web version of this article).

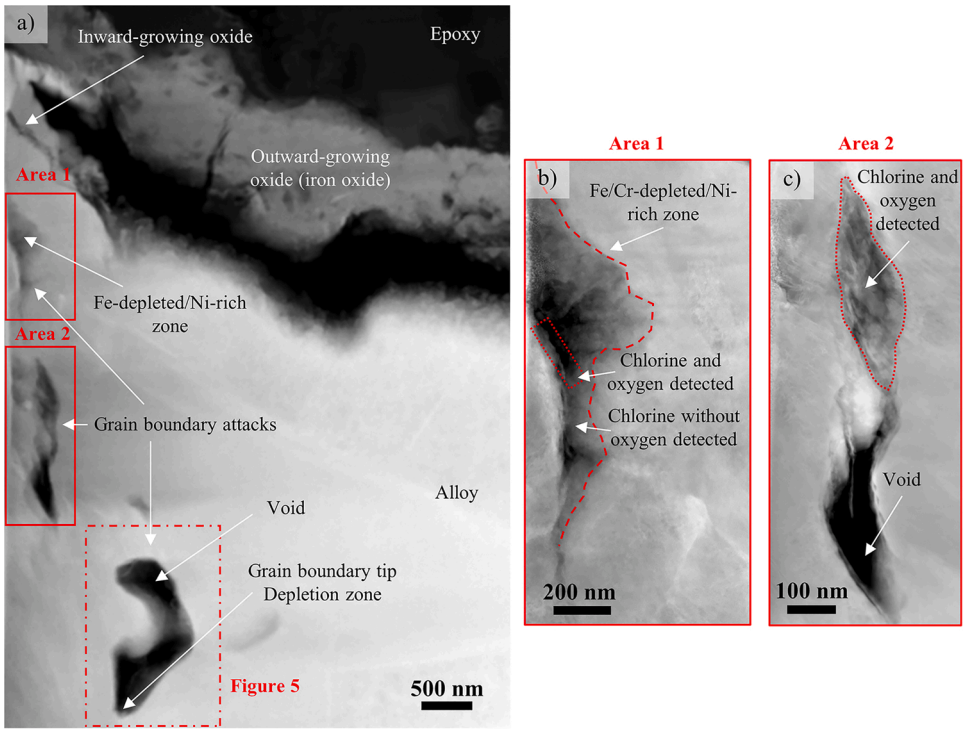

Fig. 3. High-angle annular dark-field scanning TEM (HAADF-STEM) micrographs showing the a) thin lamella of a 304 L sample exposed to 5% O_2 + 20% H_2O + N_2 (bal.) under continuous KCl deposition at 600 °C for 1-h (red box labelled "TEM lamella" in Fig. 1); b) high magnification image of the beginning of the GB attack, close to the metal/oxide interface and c) high magnification image of the apparent middle section of the GB attack. (For interpretation of the references to colour in the Figure, the reader is referred to the web version of this article).

connected. This depth and microstructure were in good agreement with a representative GB attack region after 1-h.

The HAADF image (Fig. 3a) was complemented with STEM/EDX analysis showing that the GB region was covered by an outward-growing oxide scale characterized as iron oxide (interpreted as hematite) and a thin inward-growing FeCrNi (interpreted as spinel) oxide scale of 300 nm thickness. The GB attack in the lamella could be segmented into three separate voids. The voids in Fig. 3a marked with red rectangles 1 and 2, i.e. representing the outer part of the void (1) and the middle part of the void (2), were investigated in detail. The STEM/EDX analysis revealed a depletion zone next to the void as well as traces of Cl (up to approximately 1 at. %) with and without low levels of oxygen (up to 28 at. %). Representative STEM/EDX line scan profiles across the GB void regions are shown in Fig. 4a and b. Although STEM/EDX offers high signal-to-background ratio and resolution, limitations were found in some thin regions. Thus, special effort was made to identify elements when present at low concentrations, e.g. Cl where the spectrum showed a clear peak. The results showed a Fe-Cr depletion zone of about 600 nm and 300 nm in area 1, i.e. closest to the surface. High nickel content was subsequently observed in these depletion zones. The compositional variation of different elements was compared with the alloy composition in order to be able to determine the depletion zones. The 2D representation of the complex 3D structure may overestimate the depletion zones. A large number of line scans were therefore performed and analyzed.

A similar investigation was performed in area 2, i.e the middle part of

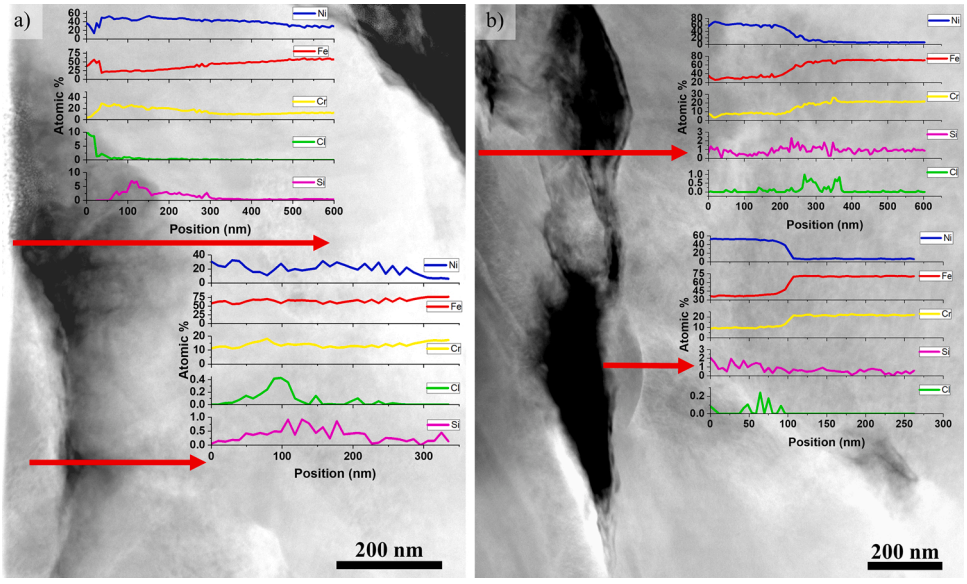

Fig. 4. High magnification HAADF-STEM micrographs (a, b) of Fig. 3b) and b) Fig. 3c) with corresponding STEM-EDX line scans (at. %), the red arrows shows the direction of the line scan. (For interpretation of the references to colour in the Figure, the reader is referred to the web version of this article).

the GB attack (see, Fig. 4b). It revealed the same type of features including traces of Cl (up to approximatively 1 at.%) with oxygen. The Fe-Cr depletion zone surrounding the void in area 2 had a similar profile to the depletion zone in area 1 with high content of Ni, reaching approximately 110 nm and 300 nm.

The void marked with a dotted rectangle in bottom right of Fig. 3a was presumed to be in/close to the tip of the GB attack. A high magnification HAADF image of this void is shown in Fig. 5a. A STEM/EDX line scan was performed across the alloy, at the bottom of the void of the GB attack (see Fig. 5b). The line scan showed small amounts of chlorine together with oxygen and a Fe-Cr depletion zone along with high Ni content were found (see Fig. 5c).

Grain boundaries located close to (within 1 μm) and further away from (> 3 μm) the corrosion front with a varying width were also characterized using STEM/EDX to investigate their composition and accumulations of impurity atoms, in particular. The width of a GB is considered to be in the nanometer range, however, during data acquisition, because of certain geometrical limitations, e.g. the geometry of the GB/foil and non-perpendicular electron beam, etc. may overestimate these measurements. An overestimate would result in a wider apparent GB. The results revealed a nominal alloy composition across and within the grain boundaries except for some minor inclusion of sulphur impurity (approximatively 2 at.%) at a one location. No crystallographic defects were observed underneath the GB attack or in the base material.

3.2. 24-h exposure - propagation

3.2.1. SEM analysis: plan view and cross-section

The optical inspection revealed substantial deposition of KCl(s) on parts of the samples after 24-h. The SEM/BSE plan view in Fig. 6a displays a section of the surface mostly covered with crystals of KCl(s) with some iron oxide protruding in between the crystals. No potassium chromates were observed, while bright rods were seen.

The largest crystals of KCl(s) were gently removed after the plan view investigation using an air duster to make sample cross-section preparation easier. A low magnification cross-section image in (Fig. 6b) shows features in good agreement with the corrosion products observed in the plan view: a thick outward-growing oxide scale (iron oxide), and an easier-to-see inward-growing oxide scale of varying thickness and with potassium chlorides on top. The average overall oxide thickness was ~ 9 μm with the outward-growing oxide scale being on average 5 μm and the inward-growing oxide scale 4 μm. In addition to the described corrosion products, the region under KCl deposition also exhibited a deep GB attack. A GB attack is defined by deterioration along a GB usually resulting in a narrow oxidation zone or void formation. Fig. 6c indicates that the oxidation that occurred at the grain boundaries is brittle and appears slightly shattered with some porosity. Bright nodules can also be seen in the middle of the oxidation, rich in nickel according to SEM/EDX. It is also possible to see a GB attack surrounded by a wider oxidation zone due to partial oxidation of steel grains. However, the oxide formed in the narrow GB attack (or in the grain boundaries) differed from the oxide formed surrounding the grain boundaries, i.e. oxide that grows further into the alloy grains. The oxidation within grain boundaries is defined by a porous and/or shattered oxide with bright nodules, while the oxidation around the grain boundaries is not homogenous in composition as the BSE/SEM image shows both dark and bright regions within the oxide (see Fig. 6c).

A GB attack, such as the one in the 2D image can reach a wide range of depths, ranging from 8 to 50 μm. However, the 2D SEM/EDX investigation did not reveal any major differences between the deep and shallow GB corrosion attacks; both exhibited oxidation at the grain boundaries with bright nodules, sometimes with an oxidation zone going into the steel grain, sometimes being narrower.

Fig. 6c illustrates a typical GB region. The marked region (green box)

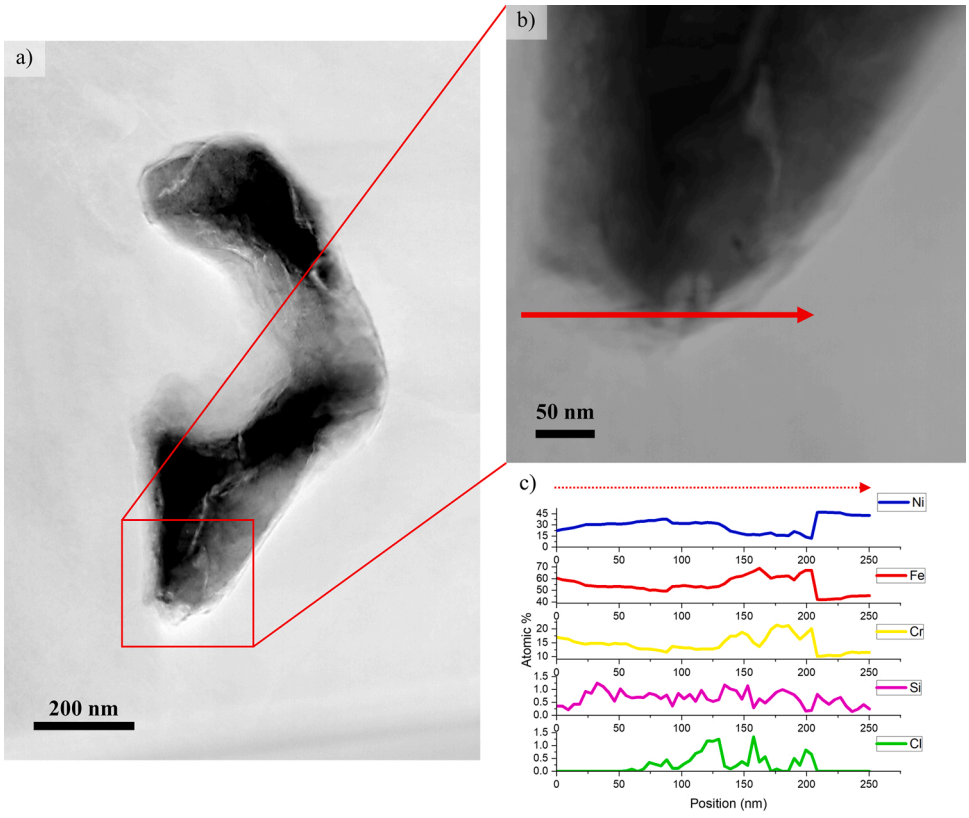

Fig. 5. a) High magnification HAADF-STEM image of the lower region of the GB attack in Fig. 3a (dotted red square); b) high magnification of the apparent tip of the GB attack and c) result of the STEM-EDX line scan (at.%)., red arrows in b and c shows the direction of the line scan. (For interpretation of the references to colour in the Figure, the reader is referred to the web version of this article).

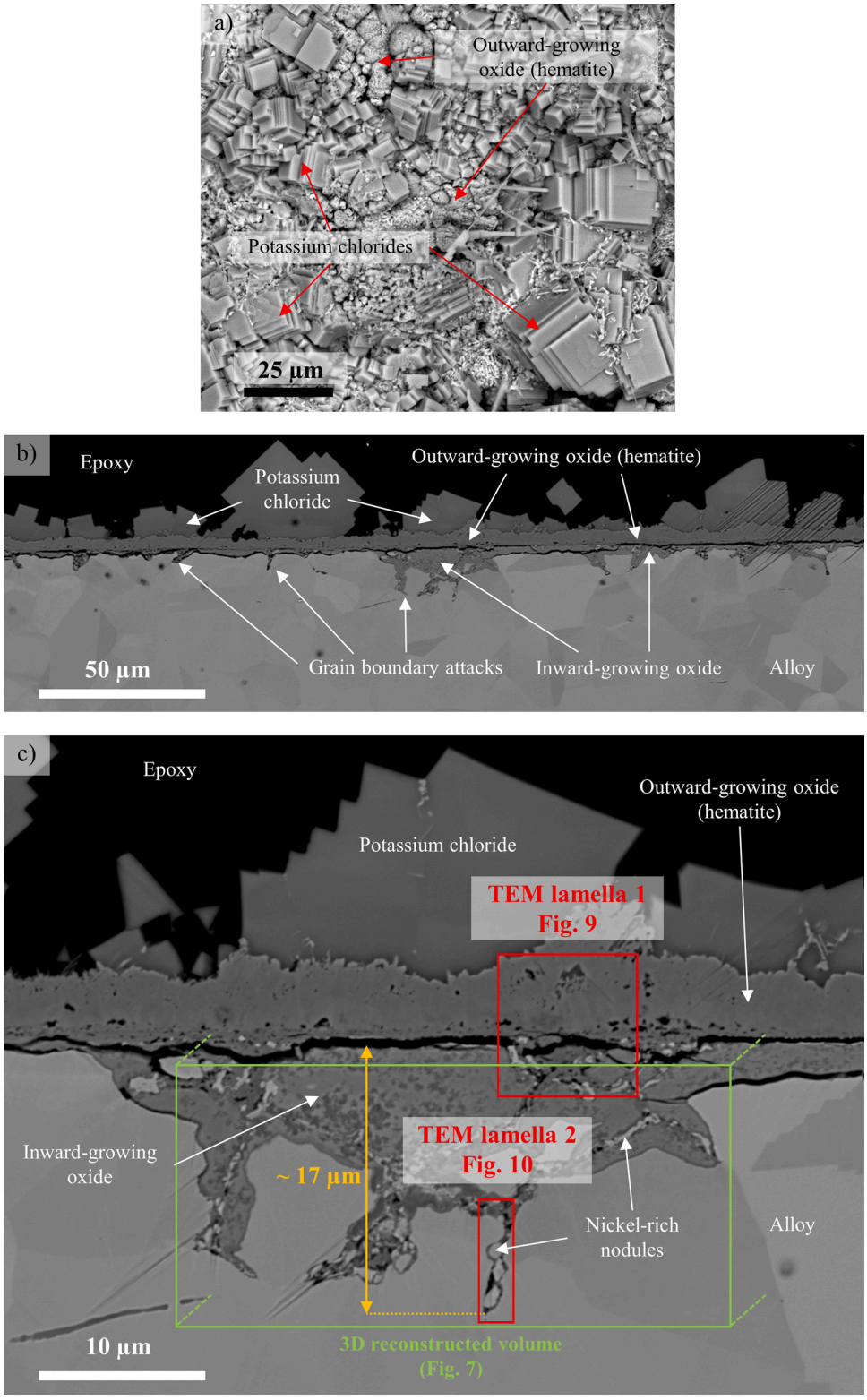

Fig. 6. BSE-SEM micrographs showing the plan view (a), low magnification (b) and high magnification (c) cross-sectional image of a 304 L sample exposed to 5% O_2 + 20 % H_2O + N_2 (bal.) under continuous KCl deposition at 600 °C for 24-h. The green box refers to the area and volume investigated via 3D tomography (Fig. 7). The red box labelled "TEM lamella 1" refers to a typical metal/oxide interface area investigated via TEM (Fig. 9). The red box labelled "TEM lamella 2" refers to a typical GB attack area investigated via TEM (Fig. 10). The yellow arrow refers to the maximum depth of the GB attacks in this area. (For interpretation of the references to colour in the Figure, the reader is referred to the web version of this article).

refers to the area and volume investigated via 3D tomography, while the marked red box labeled "TEM lamella 1" refers to a typical metal/oxide interface area investigated via TEM (Fig. 9). The marked red box labeled "TEM lamella 2" refers to a typical GB attack area investigated via TEM (Fig. 10). The yellow arrow refers to the maximum depth of the GB attacks in this area.

3.2.2. 3D tomography analysis

The result from a representative GB attack is shown in Fig. 7. The connectivity of the pores between the inward/outward-growing oxide interface and the tips of the GB attacks were investigated for the samples exposed for 24-h. The blue mesh represents all voids (connected and not connected to the surface), and the yellow mesh represents the bright nodules (nickel-rich nodules). The yellow measurement annotation

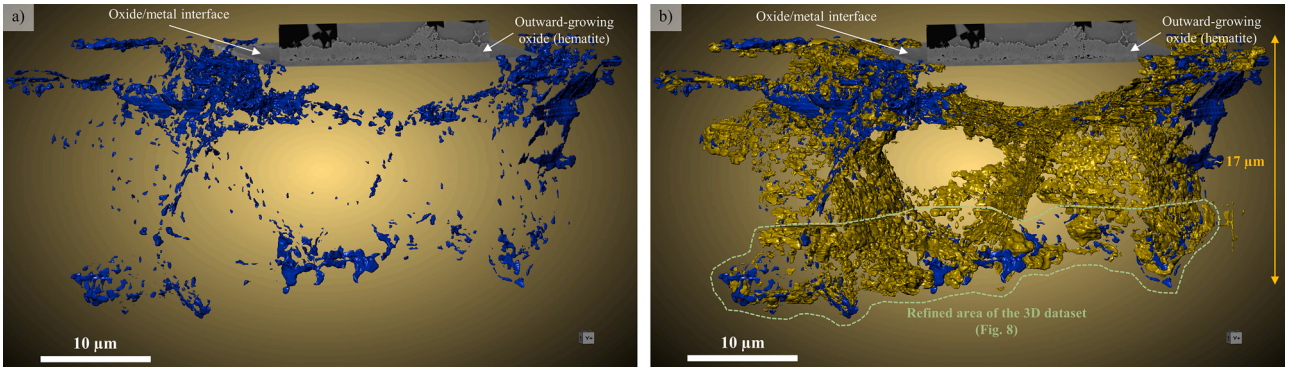

Fig. 7. a) 3D reconstruction of voids from the area highlighted with green box in Fig. 6c after 24-h of exposure and b) the same 3D reconstruction with the addition of the nickel-rich nodules/network. The blue and yellow mesh represents the voids and the nickel-rich nodules/network, respectively. The dashed green area shows the part of the dataset used in Fig. 8. (For interpretation of the references to colour in the Figure, the reader is referred to the web version of this article).

refers to the maximum depth of the GB attacks in this area. A 2D SEM image using a BSE of the outward-growing oxide scale as well as the oxide/metal interface are shown to make the illustration of the results easier to interpret. The 3D representation shows that the voids did not spread uniformly from the metal/oxide interface to the tips of the GB attack (corrosion front) as the region between these two features does not show any voids, see Fig. 7a A higher concentration of voids could be observed at the metal/oxide interface and at the tips of GB attacks. This also implies that the voids present at these two locations are not connected, meaning that the voids at the corrosion front were isolated after 24-h of exposure. Fig. 7b shows the same region as in Fig. 7a with the addition of bright nodules (nickel-rich nodules). It can be observed that these nodules form a network at the grain boundaries, consequently, surrounding the steel grains and exhibiting a depletion of iron/chromium.

The marked green box of the dataset (corrosion front) in Fig. 7b is shown in higher magnification in Fig. 8. This part of the analysis aimed at determining the morphology at the corrosion front after 24-h of exposure, i.e. during oxidation propagation. The blue and yellow mesh represent voids and bright nodules, respectively. The semi-transparent purple mesh represents the oxide. The three tips/fronts of the GB attack (Fig. 8b, c and d) were imaged at higher magnification. It can be seen in the figure that a part of the blue mesh was uncovered at the tip/corrosion front (green circles). This implies that the void/cavity is in direct contact with unoxidized metal. Oxidation was also present at the bottom of one tip, surrounding the void.

3.2.3. *TEM analysis*

Several TEM lamellas were produced to investigate a GB attack after a 24-h exposure in detail, as the attack was up to approximately 17 µm deep. Fig. 9 a shows a HAADF image of the outward- and inward-growing oxide scale on top of a typical GB. The aim was to characterize the scale formed on top of the GB, including the cracked and complex inward-growing oxide. Qualitative and quantitative analyses were performed using STEM/EDX line scan, maps, and point analysis to identify the elemental distribution across the complex oxide scale. The outward-growing oxide scale was characterized as iron oxide (interpreted as hematite) with STEM-EDX above an inward-growing FeCrNi (interpreted as spinel) oxide scale with localized distribution of about 50–65% Cr, 30–50% Fe, 1.5–9% Ni (cationic). The inward-growing oxide scale can be divided into two different regions: an outer uniform region, less cracked and attached to the outward-growing iron oxide; while the inner region was non-uniform, detached, and cracked. The grey and bright phases within the detached part of the inward growing oxide shown in Fig. 9 (b and c) correspond to a Cr/Fe-rich oxide and Ni-rich nodules, respectively. The size of these nodules can reach up to 600 µm (Fig. 9c). It is important to consider that the Ni-rich phase appears as nodules in two dimensional images but forms a network as mentioned in the 3D tomography analysis. The size of the nodules stated previously therefore refers to the diffusion length of iron and chromium.

Fig. 10 shows a HAADF image of the FIB lamella lifted out from the GB attack just beneath the uniform corrosion front, i.e. the first part of the GB attack. The aim was to characterize the middle and tip of the GB attack, and the selected region of interest for thin lamella was approximately 8 µm deep beneath the thick oxide scale. Three different regions were observed across the propagation of the GB attack within the alloy. The quantitative distribution of chemical composition among the different regions in the GB attack is shown in Fig. 10. Small traces of Cl (marked with a red dotted circle) were observed in the middle part. The iron and chromium contents in the oxide composition varied between approximatively 30–80 at.% and 20–70 at.% respectively, depending if the oxide was more chromium- or iron-rich. The bright nodule consists of Ni-rich precipitate.

Fig. 11a shows a HAADF image of a lamella made to further characterize the corrosion front as well as the GB ahead of the front of the GB attack. The void marked with the red dotted rectangle 1 in Fig. 11a was presumed to be a cross-section of a GB attack close to the corrosion front. A high magnification image of this area is shown in Fig. 11b, and an EDX line scan of the cross-section was performed. Very small amounts of chlorine were identified together with a small Fe/Cr-depletion zone along with high Ni content was observed in the line scan (see Fig. 11c). An in-depth analytical investigation within the attacked GB (Fig. 11d) in front of the corrosion fronts revealed large local variations with depletion of especially iron in combination with low concentrations of Cl (below 1 at. %) with oxygen, sulphur (below 1 at. %).

Additional investigations were performed along the path of the grain boundaries just beneath and 3 µm away from the corrosion fronts, which is 6 µm deeper down in the alloy from the inward-growing oxide scale. The investigations were conducted using STEM/EDX line scans to track the diffusion footprints, and they revealed a gradual decrease in Fe and Cr content and a subsequent increase in sulphur as it approached the grain boundaries (see Fig. 11b and c). Small levels of chlorine were also detected at the tip of GB attacks (see Fig. 11d). A local large segregation of sulphur (up to a max. of 15 at.%) impurity was observed within the grain boundaries closer and further away from the corrosion front (see Fig. 11a). In addition, small precipitates rich in Si were observed at one GB. A high magnification image of such an area (marked with red dotted rectangle 2 in Fig. 11a) is shown in Fig. 11e. In this particular GB region, the composition of the Si-rich precipitates was approximatively 63 at.% Fe, 17 at.% Cr, 15 at.% Ni, 4 at.% Si, and <1 at.% S. The depletion of

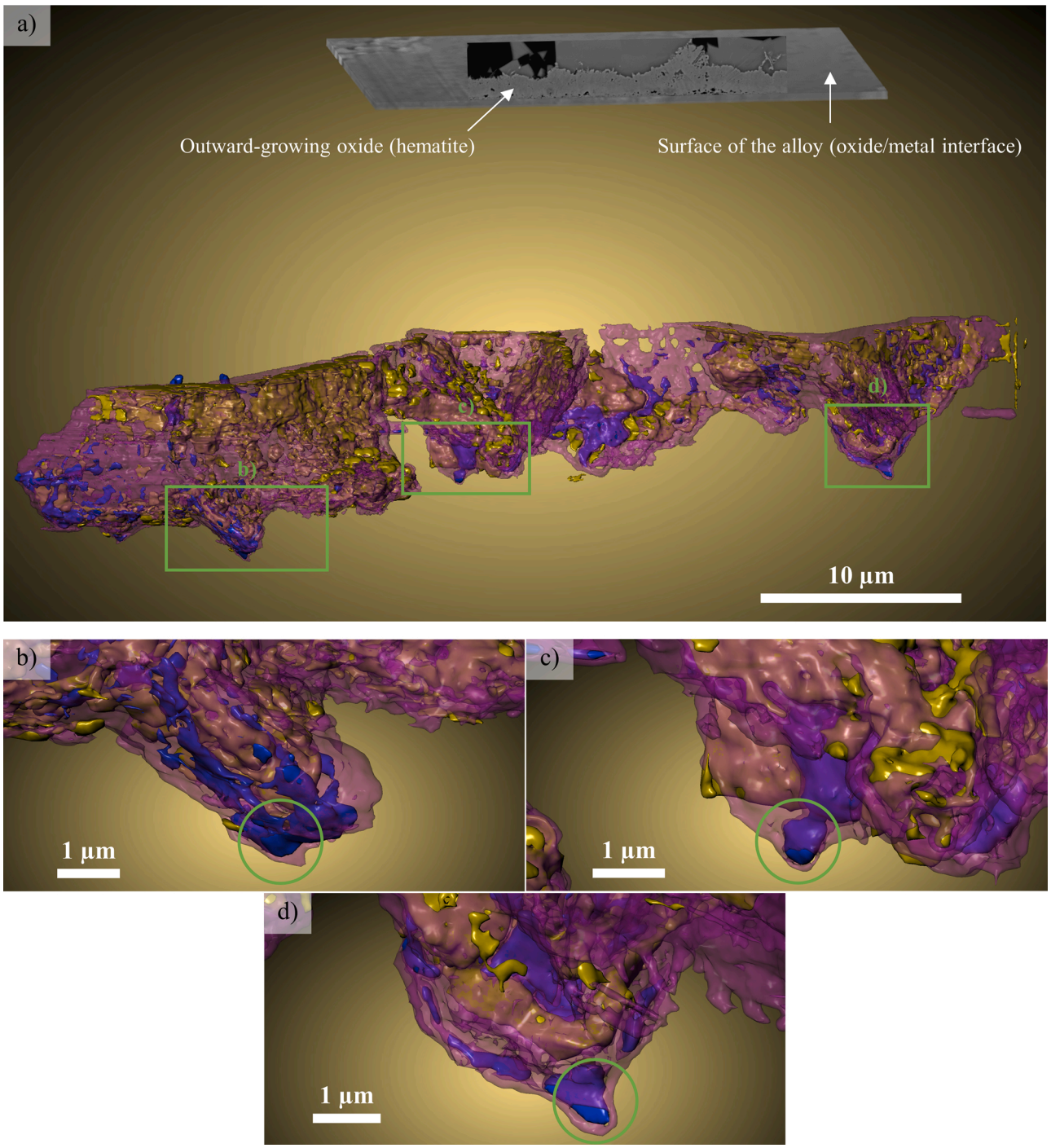

Fig. 8. a) 3D reconstruction of the part of the dataset highlighted with green dashed line in Fig. 7b; close-up images (b–d) of three tips of the GB attacks marked with green boxes in Fig. 8a. The blue and yellow mesh represents the voids and the nickel-rich nodules/network, respectively. The semi-transparent purple mesh represents the internal oxide, and green circles represent the corrosion front of the GB attacks. (For interpretation of the references to colour in the Figure, the reader is referred to the web version of this article).

chromium and enrichment of nickel took place in such a region and the Si content was higher than the original alloy composition (0.5 at.%). Thus, a segregation of both trace elements, sulphur and silicon, was observed at different locations of the investigated apparent grain boundaries after a 24-h exposure. No indications of carbide formation were observed in any of the analysis.

4. Discussion

4.1. General observations - primary and secondary corrosion regimes

Breakaway oxidation is an important feature to be considered in the high-temperature corrosion of stainless steels in demanding environments. Prior to breakaway oxidation, stainless steels form a slow

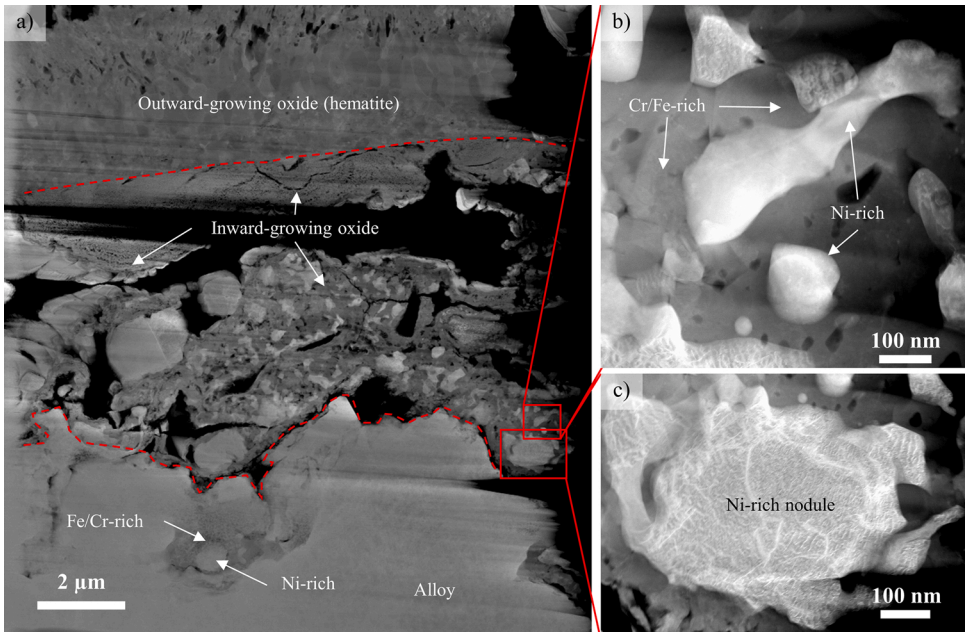

Fig. 9. HAADF-STEM micrographs showing the a) thin FIB lamella representing the metal/oxide interface of a 304 L sample exposed to 5% O_2 + 20% H_2O + N_2 (bal.) under continuous KCl deposition at 600 °C for 24-h (red box labelled "TEM lamella 1" in Fig. 6c; b) high magnification image of a typical inward-growing oxide region showing Cr-rich (in grey) and Ni-rich areas (in bright); c) high magnification image of a Ni-rich nodule. (For interpretation of the references to colour in the Figure, the reader is referred to the web version of this article).

growing Cr-rich oxide scale on top of the alloy, thus, protecting the substrate material from the environment [52–57]. This oxide scale exhibits properties beneficial for the protection of the underlying material, such as slow growing, dense and adherent, resulting in slow oxidation and therefore little loss of the substrate material. This material behavior prior to breakaway oxidation may be referred to the primary regime [58].

In contrast, when a material reaches breakaway oxidation, the protectiveness of the initial protective thin oxide has been lost. This usually results in the growth of a less protective oxide scale, showing higher corrosion rates. The growth of the scale formed after breakaway oxidation may be referred to the secondary regime [58]. In this regime, further growth of the secondary oxide scale may also occur via ion diffusion. However, the properties of the secondary oxide scale are generally defined by the presence of a poorly protective iron oxide scale. These differences between the primary and secondary regimes show the divergence in corrosion rates (higher in the secondary regime).

It has been shown that alkali, even in small amounts, triggers very rapid breakaway oxidation of the primary oxide scale formed on the stainless steel 304 L and that the protection is dominated by the secondary protection regime [12,18,59,60]. The behavior following breakaway is defined by the growth of a fast-outward-growing iron oxide scale and an inward-growing spinel oxide scale (secondary regime). However, by adding KCl in larger amounts (e.g. via continuous KCl deposition *in-situ*), deep alloy GB attack is observed, together with the formation of the secondary oxide (i.e. inward-growing spinel oxide and outward-growing oxide), see Fig. 6 [30]. It should be noted that the deep grain boundary attack was only associated with regions covered by large amounts of KCl deposited and that a diffusion-controlled secondary regime was observed on other parts of the surface [30].

4.2. Initiation of a grain boundary attack

The SEM-BSE/TEM images show that the initial corrosion attack consisted of an outward-growing iron oxide scale on top of an inward-growing Fe,Cr,Ni oxide scale, i.e. indicating an ion diffusion-controlled secondary protection. Beneath this scale, the GB attack had reached a depth up to ~3 µm after only 1-h of exposure. The 3D-FIB/TEM investigation showed that the GB attack during the initial attack was characterized by voids with very little oxidation/chlorination, especially at the apparent tip of the attack (see Fig. 5). The 3D tomography analysis revealed that 96% of these voids were directly connected to the metal/oxide interface, which can be interpreted as fast pathways for the gas transport and/or ion diffusion of species on the surfaces surrounding the voids. The open, connected pore network in the GB regions, the absence of large oxide formation in the same regions, and the expected increase in Cl load below the deposited KCl regions may indicate the presence of the volatile iron/chromium chlorides associated with the active oxidation mechanism [7,11,22–27]. Only at one position (outer void in the TEM investigation), higher levels of Cl (about 10 at.% associated with Fe/Ni) were observed, see Fig. 3b. However, no local accumulation of iron oxide was detected in the top part of the empty GB regions. Instead, the investigation revealed an intact secondary oxide scale that seemed to remain diffusion controlled as no severe degradation of the oxides was observed, i.e. indications of cracks and/or accumulation of oxide pores, see Fig. 3. Instead, the detailed TEM analysis showed the presence of surprisingly long depletion zones in the vicinity of the GB attack. These zones were larger close to the metal/oxide interface (300−600 nm, see Fig. 4a) and shorter close to the tip of the GB attack (110−300 nm, see Fig. 4b). If the GB attack would be progressing by a gaseous attack (and not diffusion-controlled), it would be expected that the depletion zones in connection to the voids would be equally long, regardless of distance to the surface since a gaseous attack occurs instantaneously throughout the entire void.

The 2D representation of the 3D voids may however somewhat overestimate the length of the depletion zones. A large number of analysis were therefore performed and interpreted to verify the approximate lengths. It should be noted that the depletion zones were associated with very small levels of Cl. The presence of Cl was identified by investigating the EDX data (peaks/noise ration) and not by quantification, even though the results are presented as at.% in the line scans in order to illustrate the presence of Cl. Both iron and chromium were depleted, and nickel accumulated in these regions. Several alloy GB regions ahead of the corrosion front were investigated, and their composition was found to be similar to the original composition of the alloy even if some Cl could be detected in the GB ahead of the corrosion front. Similar large depletion zones of iron and chromium have previously been reported for the stainless steel Sanicro28 after exposure to a similar environment [61].

The bulk and GB diffusivities of chromium in 304 L at 600 °C were predicted using data depletion zones from a stainless steel at different temperatures to interpret the depletion zones. After a one-hour exposure

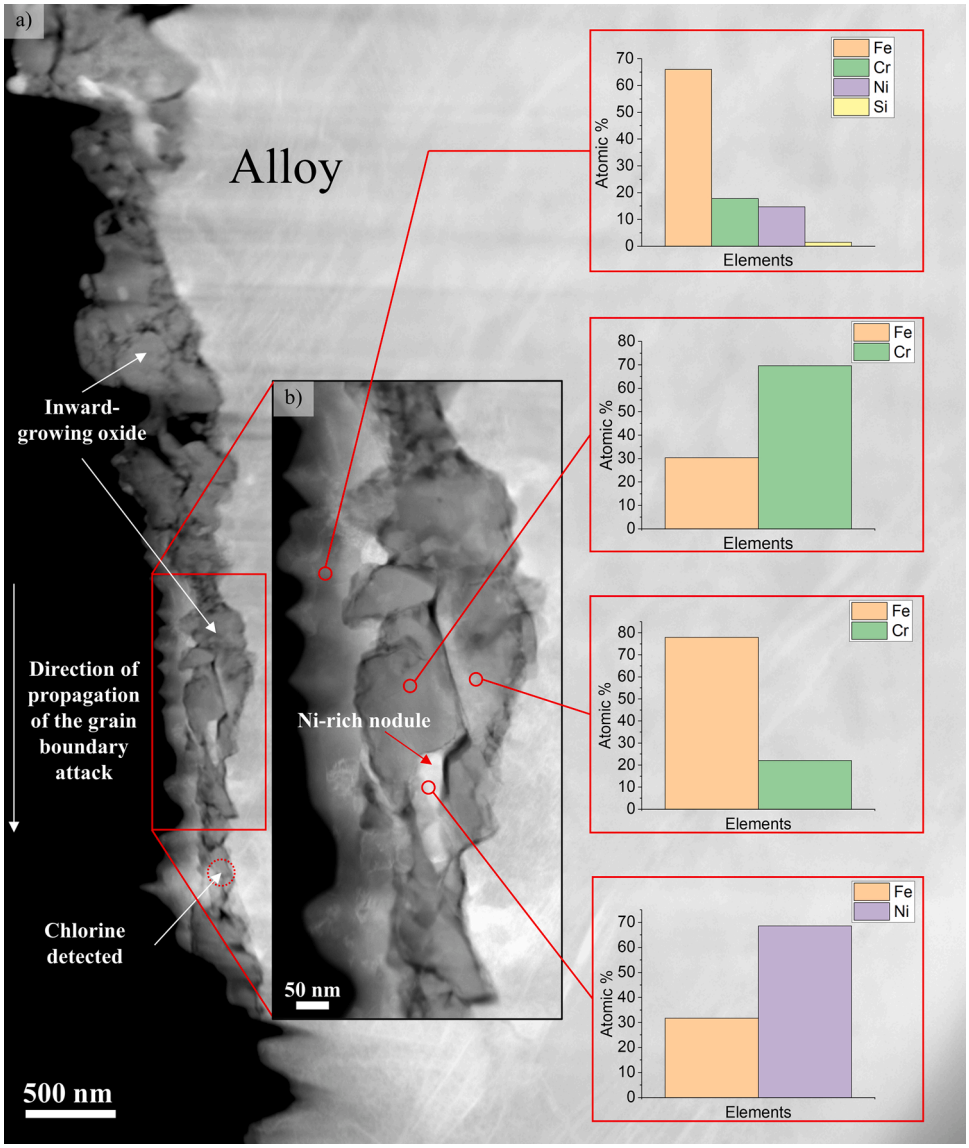

Fig. 10. HAADF-STEM micrograph of a thin foil a) lower and b) high magnification image of a GB attack from a 304 L sample exposed to 5% O_2 + 20% H_2O + N_2 (bal.) under continuous KCl deposition at 600 °C for 24-h (red box labelled "TEM lamella 2" in Fig. 6c. Locations of quantitative analysis are marked with red lines and their corresponding results are represented in at. %. (For interpretation of the references to colour in the Figure, the reader is referred to the web version of this article).

at 600 °C, the calculated depletion zone using bulk diffusivity was in the range of a few nanometers, i.e. several orders of magnitude lower than the depletion zones measured in this study (from the GB region and into the neighboring alloy grain). The length of the depletion zones in connection to the grain boundaries of the 304 L in this study, i.e. exposed to a KCl-rich environment at 600 °C, may be compared to the behavior of materials exposed to higher temperatures where the diffusivity would be higher. In the article referred to [62], large empty voids are seen at alloy grain boundaries although the environment contains no Cl but the exposure temperature is higher, 800 °C. Thus, the results indicate that a local enrichment of Cl at the GB regions may increase the diffusivity of alloying elements, similar to what is achieved by increasing the temperature. Initially increasing the diffusivity in GB regions promotes the formation of voids and thereby new surfaces where fast surface diffusion is expected. Accumulations of Cl (metal chlorides) on top of GB regions has earlier been observed with TEM during the initial oxidation of a stainless steel exposed at 500 °C in the presence of HCl [23]. A similar sample preparation/handling approach was used in this study, which found that no large amounts of metal chlorides were lost during sample preparation. The results of the microstructural investigation gave a good representation of the Cl distribution at the GB attack.

4.3. Propagation of the grain boundary attack

The SEM-BSE/TEM investigation showed the presence of a thicker scale after a 24-h exposure with the same type of microstructure covering the alloy as earlier (the diffusion-controlled oxide scale), i.e. secondary protection. The thickness of the secondary oxide scale was in the same range as an oxide scale formed on regions without any alloy GB attack [30]. However, the inward-growing oxide scale on top of the alloy GB regions exhibited two domains: a top part that was a homogeneous oxide layer attached to the outward-growing oxide scale, and another part that was heterogenous with a chromium/iron-rich matrix with large nickel-rich nodules, see Fig. 9. This type of morphology has been observed in the corrosion front of the 304 L steel after a 24-h exposure to several environments (i.e. Fe-Ni metal mixed with the internal oxidation of Fe-Cr oxide) on a much smaller scale [12,63]. The SEM/BSE images indicate the presence of this type of microstructure (light grey part of the

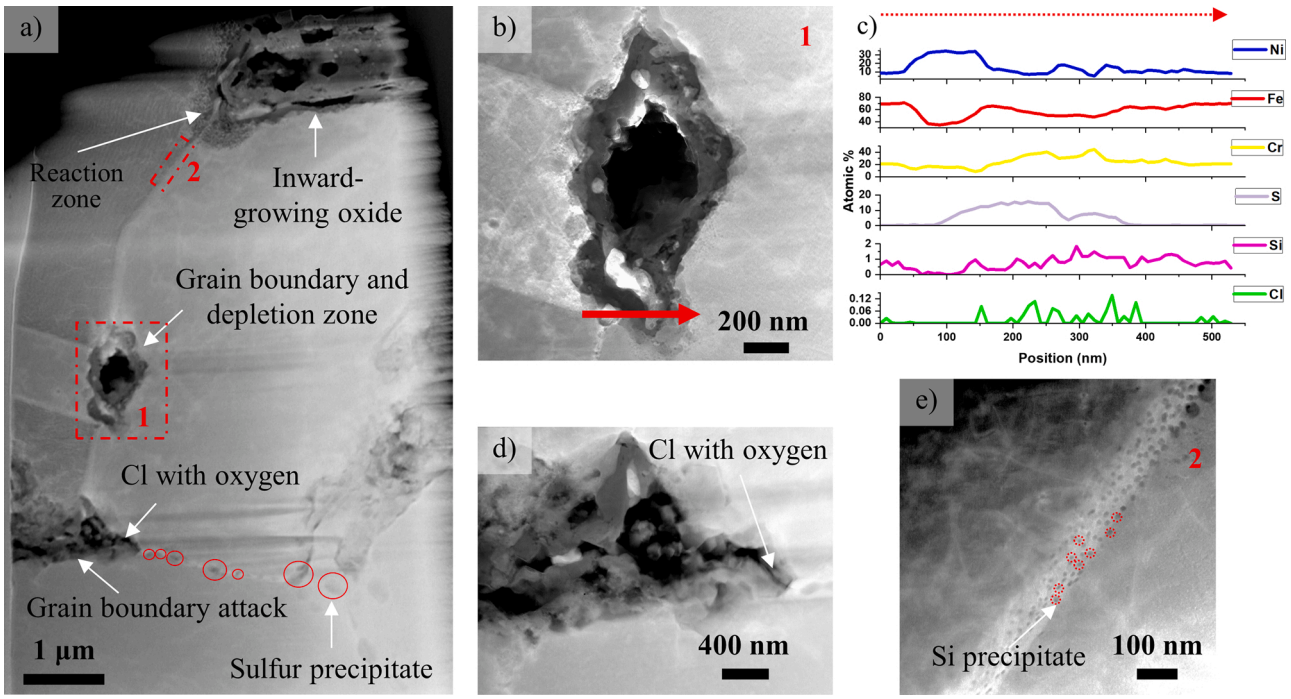

Fig. 11. HAADF-STEM micrographs showing the a) thin foil; b) high magnification image of the void considered to be a cross-section of GB attack and red arrow showing the direction of the line scan; c) line scan profile showing the distribution of different elements (at. %); d) high magnification of the tip of the highly attacked region and e) segregation of Si precipitates at a non-attacked GB. (For interpretation of the references to colour in the Figure, the reader is referred to the web version of this article).

inward-growing oxide scale) in the middle of alloy grains, see Fig. 6. However, TEM is required to reveal the fine details of the microstructure.

After 24-h, the GB attack showed a wide range of depths (8–50 µm, see Fig. 6 and [30]). The growth rate of the GB attack after initiation (1-h) remained high even if it was challenging to determine a typical growth rate due to the complex 3D structure of a GB. After the initial hour of exposure, a GB attack that was up to 3 µm down from the surface was observed, while the attack had reached 50 µm after 24-h. The 3D tomography analysis revealed the presence of voids close to the interface of the alloy/secondary oxide scale and at the tips of GB attack (approximatively at 17 µm from the interface of the secondary oxide scale). However, no clear connections between these two clusters of voids were observed after 24-h as the middle/upper parts had been oxidized. This contradicted the potential of connected voids to be considered as fast pathways for gas phase transport of species. The middle part of the grain boundaries was filled with brittle/shattered oxide and nickel-rich nodules. The network of Ni-rich nodules was observed in the 3D representation, see Fig. 7b, that covered a large fraction of the GB regions. The Ni-rich nodules are larger closer to the metal/oxide interface and appeared to be formed by diffusion of iron and chromium to form the oxide detected within the grain boundaries. The TEM analysis showed that the Ni-rich nodules contained some iron and that the oxide found in the grain boundaries was heterogeneous in composition, i.e. either iron- or chromium-rich, see Fig. 10. The presence of trace amounts of Cl was once more detected with oxygen within such a GB. The absence of nickel in the oxide of the GB regions indicates that the activity of oxygen is below 10^{-21} (using thermodynamic calculations) in these regions [12]. This implies that the secondary oxide scale on top of the GB regions as intact as the oxygen activity remained low below this scale.

The investigation of the alloy GB regions after a 24-h exposure showed a microstructure indicating fast diffusion (larger expected features in a diffusion-grown microstructure) at and in the vicinity of the alloy grain boundaries, see Fig. 6c. The 3D information in addition revealed large Ni-rich regions (Ni/Fe metal shown with TEM). The 3D analysis indicated that voids were present at the GB corrosion front. The microstructure of the oxide scales formed in the formerly empty GB regions indicates a diffusion grown scale with varying Cr/Fe ratios. This would be expected since some parts of the 1-h exposure must have been depleted of Fe/Cr prior to oxidation, see results from 1-h exposure in Fig. 4a and b. Cl was again detected close to the corrosion front as well as in the GB ahead of the corrosion front even if the presence of Cl was harder to determine after longer exposure times due to the complex structure and the small amounts. The results in addition showed that trace elements from the alloy had accumulated at the alloy grain boundaries after 24-h, see Fig. 11a and e. This would be expected after longer exposure times at higher temperatures, and this accumulation would be expected to increase the diffusivity at grain boundaries. However, no indications of any Cr-rich phases (e.g. carbides) were observed.

4.4. *Beyond secondary protection – Alloy grain boundary attack*

A deep GB attack can drastically increase material degradation due to the loss of sound material, even if a grain has not been fully oxidized, see e.g. [31]. A deep GB attack implies that other corrosion mechanisms are involved in the corrosion attack, i.e. another regime of corrosion has begun. The literature survey in combination with the present findings indicate that this type of material degradation can be caused by high temperature [62] or a combination of temperature and environment. The ageing of material and the formation of, e.g. a Cr-rich precipitate, have been suggested to cause a selective attack. However, no indication of this behavior (formation of carbides) was found in the present study [64].

The oxide microstructure formed after breakaway has been described to be generic for a wide set of FeCr, FeCrNi and FeCrAl alloys [58]. This implies that corrosion after breakaway can be modeled similarly for many Fe-based alloys using generalized modeling tools. However, the very localized material degradation below an intact

secondary scale described in the present study must be accounted for. It is necessary to improve the understanding of the corrosion mechanisms in corrosion beyond the secondary corrosion regime in order to better predict the corrosion behavior of materials. However, the very localized and complex geometry and/or small scale of the corrosion attack makes this a challenge to study. This study shows that a combined 3D-FIB/TEM investigation has a great potential in investigating and characterizing such a complex corrosion attack.

5. Summary

This study provides new insights into intergranular corrosion in stainless steels through a detailed representation using FIB/SEM to perform 3D reconstruction/tomography of GB attacks linked to a TEM investigation.

The key findings are:

- The combination of the 3D-FIB/TEM has great potential for the study of complex features, i.e. intergranular corrosion. 3D tomography provides information beyond the traditional two-dimensional analyses thus allowing for improved interpretation of the features observed, while the TEM complements with high magnification imaging and high-resolution chemical analysis. The implementation of the 3D EDX-FIB technique in future work would enhance the depth of such a study by providing three-dimensional chemical information.
- The initiation (1-h exposure) and growth (24-h exposure) of the GB attack occurred very rapid below an intact secondary diffusion-controlled protection.
- No large accumulations of metal chlorides were found at the GB regions. Instead, indications of rapid diffusion (large depletion zones) and a microstructure indicating fast diffusion were observed.

Data availability

The raw/processed data required to reproduce these findings cannot be shared at this time due to technical or time limitation.

CRediT authorship contribution statement

J. Phother-Simon: Conceptualization, Methodology, Validation, Formal analysis, Investigation, Writing - original draft, Resources, Visualization. **I. Hanif:** Conceptualization, Methodology, Validation, Formal analysis, Investigation, Resources, Writing - original draft, Visualization, Writing - review & editing. **J. Liske:** Conceptualization, Writing - review & editing, Supervision. **T. Jonsson:** Conceptualization, Writing - review & editing, Supervision.

Declaration of Competing Interest

The authors declare that they have no known competing financial interests or personal relationships that could have appeared to influence the work reported in this paper.

Acknowledgments

This work was carried out at the Swedish High Temperature Corrosion Centre (HTC) and in part at the Chalmers Material Analysis Laboratory (CMAL) at Chalmers University of Technology and is hereby gratefully acknowledged together with its member companies (Sandvik Materials Technology, Sandvik Heating Technology, Energiforsk (represented by Vattenfall, E.ON Värme, Fortum Värme, Mälarenergi and Tekniska V. i Linköping) Valmet, Sumitomo SHI FW Energia Oy, Babcock & Wilcox Völund, Andritz, and Castolin). Financial support from Chalmers Area of Advance Energyand material supply from Outokumpuare also acknowledged.

References

[1] E.O. Värme, Change of Fuel Composition From 1991 to 2019 in Händeloverket, E. On internal data, 2020.
[2] S. Karlsson, L.-E. Åmand, J. Liske, Reducing high-temperature corrosion on high-alloyed stainless steel superheaters by co-combustion of municipal sewage sludge in a fluidised bed boiler, Fuel 139 (2015) 482–493.
[3] H. Kassman, L. Bäfver, L.-E. Åmand, The importance of SO2 and SO3 for sulphation of gaseous KCl – An experimental investigation in a biomass fired CFB boiler, Combust. Flame 157 (9) (2010) 1649–1657.
[4] H. Kassman, M. Broström, M. Berg, L.-E. Åmand, Measures to reduce chlorine in deposits: application in a large-scale circulating fluidised bed boiler firing biomass, Fuel 90 (4) (2011) 1325–1334.
[5] H. Kassman, J. Pettersson, B.-M. Steenari, L.-E. Åmand, Two strategies to reduce gaseous KCl and chlorine in deposits during biomass combustion—injection of ammonium sulphate and co-combustion with peat, Fuel Process. Technol. 105 (2013) 170–180.
[6] A.T. Masiá, B. Buhre, R. Gupta, T. Wall, Characterising ash of biomass and waste, Fuel Process. Technol. 88 (11–12) (2007) 1071–1081.
[7] H.P. Nielsen, F.J. Frandsen, K. Dam-Johansen, L.L. Baxter, The implications of chlorine-associated corrosion on the operation of biomass-fired boilers, Prog. Energy Combust. Sci. 26 (3) (2000) 283–298.
[8] S.V. Vassilev, D. Baxter, L.K. Andersen, C.G. Vassileva, T.J. Morgan, An overview of the organic and inorganic phase composition of biomass, Fuel 94 (2012) 1–33.
[9] K.O. Davidsson, L.-E. Åmand, B. Leckner, B. Kovacevik, M. Svane, M. Hagström, et al., Potassium, chlorine, and sulfur in ash, particles, deposits, and corrosion during wood combustion in a circulating fluidized-bed boiler, Energy Fuels 21 (1) (2007) 71–81.
[10] N. Folkeson, J. Pettersson, C. Pettersson, L.G. Johansson, E. Skog, B.-Å Andersson, et al., Fireside corrosion of stainless and low alloyed steels in a waste-fired CFB boiler; The effect of adding sulphur to the fuel, Mater. Sci. Forum 595 (2008) 289–297. Trans Tech Publ.
[11] H.J. Grabke, E. Reese, M. Spiegel, The effects of chlorides, hydrogen chloride, and sulfur dioxide in the oxidation of steels below deposits, Corros. Sci. 37 (7) (1995) 1023–1043.
[12] T. Jonsson, S. Karlsson, H. Hooshyar, M. Sattari, J. Liske, J.-E. Svensson, et al., Oxidation after breakdown of the chromium-rich scale on stainless steels at high temperature: internal oxidation, Oxid. Met. 85 (5) (2016) 509–536.
[13] S. Kiamehr, K.V. Dahl, M. Montgomery, M.A.J. Somers, KCl-induced high temperature corrosion of selected commercial alloys, Mater. Corros. 66 (12) (2015) 1414–1429.
[14] J. Lehmusto, P. Yrjas, B.J. Skrifvars, M. Hupa, High temperature corrosion of superheater steels by KCl and K2CO3 under dry and wet conditions, Fuel Process. Technol. 104 (2012) 253–264.
[15] S.C. Okoro, S. Kiamehr, M. Montgomery, F.J. Frandsen, K. Pantleon, Effect of flue gas composition on deposit induced high temperature corrosion under laboratory conditions mimicking biomass firing. Part I: exposures in oxidizing and chlorinating atmospheres, Mater. Corros. 68 (5) (2017) 499–514.
[16] S.C. Okoro, M. Montgomery, F.J. Frandsen, K. Pantleon, High temperature corrosion during biomass firing: improved understanding by depth resolved characterisation of corrosion products, Mater. High Temp. 32 (1–2) (2015) 92–101.
[17] J. Pettersson, H. Asteman, J.-E. Svensson, L.-G. Johansson, KCl induced corrosion of a 304-type austenitic stainless steel at 600°C; the role of potassium, Oxid. Met. 64 (1) (2005) 23–41.
[18] J. Pettersson, N. Folkeson, L.-G. Johansson, J.-E. Svensson, The effects of KCl, K2SO4 and K2CO3 on the high temperature corrosion of a 304-type austenitic stainless steel, Oxid. Met. 76 (1) (2011) 93–109.
[19] J. Sui, J. Lehmusto, M. Bergelin, M. Hupa, The effects of KCl, NaCl and K2CO3 on the high-temperature oxidation onset of sanicro 28 steel, Oxid. Met. 85 (5) (2016) 565–598.
[20] H.P. Michelsen, F. Frandsen, K. Dam-Johansen, O.H. Larsen, Deposition and high temperature corrosion in a 10 MW straw fired boiler, Fuel Process. Technol. 54 (1) (1998) 95–108.
[21] M. Montgomery, A. Karlsson, In-situ corrosion investigation at Masnedø CHP plant–a straw-fired power plant, Mater. Corros. 50 (10) (1999) 579–584.
[22] J.M. Abels, H.H. Strehblow, A surface analytical approach to the high temperature chlorination behaviour of inconel 600 at 700 °C, Corros. Sci. 39 (1) (1997) 115–132.
[23] N. Folkeson, L.-G. Johansson, J.-E. Svensson, Initial stages of the HCl-induced high-temperature corrosion of alloy 310, J. Electrochem. Soc. 154 (9) (2007) C515–C521.
[24] M. McNallan, W. Liang, S. Kim, C. Kang, Acceleration of the high temperature oxidation of metals by chlorine, in: International Corrosion Conference Series, NACE, 1983.
[25] Y. Shinata, Accelerated oxidation rate of chromium induced by sodium chloride, Oxid. Met. 27 (5) (1987) 315–332.
[26] C.-J. Wang, T.-T. He, Morphological development of subscale formation in Fe–Cr–(Ni) alloys with chloride and sulfates coating, Oxid. Met. 58 (3) (2002) 415–437.
[27] A. Zahs, M. Spiegel, H.J. Grabke, Chloridation and oxidation of iron, chromium, nickel and their alloys in chloridizing and oxidizing atmospheres at 400–700°C, Corros. Sci. 42 (6) (2000) 1093–1122.
[28] V. Cantatore, M.A. Olivas Ogaz, J. Liske, T. Jonsson, J.-E. Svensson, L.-G. Johansson, et al., Oxidation driven permeation of Iron oxide scales by chloride from experiment guided first-principles modeling, J. Phys. Chem. C 123 (42) (2019) 25957–25966.

[29] T. Jonsson, N. Folkeson, J.E. Svensson, L.G. Johansson, M. Halvarsson, An ESEM in situ investigation of initial stages of the KCl induced high temperature corrosion of a Fe–2.25Cr–1Mo steel at 400°C, Corros. Sci. 53 (6) (2011) 2233–2246.
[30] J. Phother-Simon, T. Jonsson, J. Liske, Continuous KCl addition in high temperature exposures of 304 L – a way to mimic a boiler environment, Corros. Sci. 167 (2020), 108511.
[31] L. Mikkelsen, T. Jonsson, L. Paz, J. Eklund, J. Liske, B. Jonsson, et al., Increased steam temperature in grate fired boilers - steamboost, KME 709 (2017) 113.
[32] C.W. Bale, P. Chartrand, S. Degterov, G. Eriksson, K. Hack, R.B. Mahfoud, et al., FactSage thermochemical software and databases, Calphad 26 (2) (2002) 189–228.
[33] M. Quirynen, Y. Lamoral, C. Dekeyser, P. Peene, D. van Steenberghe, J. Bonte, et al., The CT scan standard reconstruction technique for reliable jaw bone volume determination, Int. J. Oral Maxillofac. Implants 5 (4) (1990).
[34] D.A. Roth, A.K. Gosain, J.G. McCarthy, M.A. Stracher, D.R. Lefton, B.H. Grayson, A CT scan technique for quantitative volumetric assessment of the mandible after distraction osteogenesis, Plast. Reconstr. Surg. 99 (5) (1997) 1237–1247.
[35] K. Tokunaga, Y. Matsuzawa, K. Ishikawa, S. Tarui, A novel technique for the determination of body fat by computed tomography, Int. J. Obes. 7 (5) (1983) 437.
[36] L. HOLZER, F. INDUTNYI, P. GASSER, B. MÜNCH, M. WEGMANN, Three-dimensional analysis of porous BaTiO3 ceramics using FIB nanotomography, J. Microsc. 216 (1) (2004) 84–95.
[37] B.J. Inkson, M. Mulvihill, G. Möbus, 3D determination of grain shape in a FeAl-based nanocomposite by 3D FIB tomography, Scr. Mater. 45 (7) (2001) 753–758.
[38] K. Jahns, U. Krupp, G. Sundell, C. Geers, Formation of corrosion pockets in FeNiCrAl at high temperatures investigated by 3D FIB-SEM tomography, Mater. Corros. (2020).
[39] P.G. Kotula, M.R. Keenan, J.R. Michael, Tomographic spectral imaging with multivariate statistical analysis: comprehensive 3D microanalysis, Microsc. Microanal. 12 (1) (2006) 36–48.
[40] B. Langelier, S.Y. Persaud, A. Korinek, T. Casagrande, R.C. Newman, G.A. Botton, Effects of boundary migration and pinning particles on intergranular oxidation revealed by 2D and 3D analytical electron microscopy, Acta Mater. 131 (2017) 280–295.
[41] S. Lozano-Perez, K. Kruska, I. Iyengar, T. Terachi, T. Yamada, Understanding surface oxidation in stainless steels through 3D FIB sequential sectioning, J. Phys. Conf. Ser. 371 (2012), 012086.
[42] S. Lozano-Perez, P. Rodrigo, L.C. Gontard, Three-dimensional characterization of stress corrosion cracks, J. Nucl. Mater. 408 (3) (2011) 289–295.
[43] N. Ni, S. Lozano-Perez, J.M. Sykes, G.D.W. Smith, C.R.M. Grovenor, Focussed ion beam sectioning for the 3D characterisation of cracking in oxide scales formed on commercial ZIRLOTM alloys during corrosion in high temperature pressurised water, Corros. Sci. 53 (12) (2011) 4073–4083.
[44] T. Sakamoto, Z. Cheng, M. Takahashi, M. Owari, Y. Nihei, Development of an ion and Electron Dual focused beam apparatus for three-dimensional microanalysis, J. Appl. Phys. 37 (Part 1, No. 4A) (1998) 2051–2056.
[45] S.S. Singh, J.J. Loza, A.P. Merkle, N. Chawla, Three dimensional microstructural characterization of nanoscale precipitates in AA7075-T651 by focused ion beam (FIB) tomography, Mater. Charact. 118 (2016) 102–111.
[46] J. Schindelin, I. Arganda-Carreras, E. Frise, V. Kaynig, M. Longair, T. Pietzsch, et al., Fiji: an open-source platform for biological-image analysis, Nat. Methods 9 (7) (2012) 676–682.
[47] J. Schindelin, C.T. Rueden, M.C. Hiner, K.W. Eliceiri, The ImageJ ecosystem: an open platform for biomedical image analysis, Mol. Reprod. Dev. 82 (7–8) (2015) 518–529.
[48] C.A. Schneider, W.S. Rasband, K.W. Eliceiri, NIH Image to ImageJ: 25 years of image analysis, Nat. Methods 9 (7) (2012) 671–675.
[49] (ORS) ORS, Dragonfly (Version 4.1.0.647) [Software], 2019.
[50] A. Khan, R. Srisha, Image segmentation methods: a comparative study, Int. J. Soft Comput. Softw. Eng. (2013) 2231–2307.
[51] D. Kaur, Y. Kaur, Various Image Segmentation Techniques: A. Review, 2014.
[52] H. Bhadeshia, R. Honeycombe, Steels: Microstructure and Properties, Elsevier Science, 2017.
[53] W.D. Callister, Materials Science And Engineering: An Introduction, John Wiley & Sons, 2007.
[54] D.A. Jones, Principles and Prevention of Corrosion, Prentice Hall, 1996.
[55] A.S. Khanna, Introduction to High Temperature Oxidation and Corrosion, ASM International, 2002.
[56] P. Kofstad, High Temperature Corrosion, 1988.
[57] G.Y. Lai, High-temperature Corrosion and Materials Applications, ASM international, 2007.
[58] PERSDOTTER A. Beyond Breakaway Corrosion: Secondary Corrosion Protection of Iron-based Alloys.
[59] S. Karlsson, J. Pettersson, J.-E. Svensson, L.-G. Johansson, KCl-Induced High Temperature Corrosion of the Austenitic Stainless Steel 304L–The Influence of SO2, Mater. Sci. Forum 696 (2011) 224–229. Trans Tech Publ.
[60] S.C. Okoro, M. Montgomery, F.J. Frandsen, K. Pantleon, Time and temperature effects on alkali chloride induced high temperature corrosion of superheaters during biomass firing, Energy Fuels 32 (7) (2018) 7991–7999.
[61] C. Proff, T. Jonsson, C. Pettersson, J.-E. Svensson, L.-G. Johansson, M. Halvarsson, Microstructural investigation of the KCl-induced corrosion of the austenitic alloy Sanicro 28 (35Fe27Cr31Ni) at 600 C, Mater. High Temp. 26 (2) (2009) 113–125.
[62] T. Sand, C. Geers, Y. Cao, J. Svensson, L. Johansson, Effective reduction of chromium-oxy-hydroxide evaporation from Ni-base alloy 690, Oxid. Met. 92 (3–4) (2019) 259–279.
[63] S. Karlsson, J. Pettersson, L.-G. Johansson, J.-E. Svensson, Alkali induced high temperature corrosion of stainless steel: the influence of NaCl, KCl and CaCl 2, Oxid. Met. 78 (1–2) (2012) 83–102.
[64] Y.C. Malede, J.P. Simon, T. Jonsson, M. Montgomery, K.V. Dahl, J. Hald, KCl-induced corrosion of Ni-based alloys containing 35–45 wt% Cr, Mater. Corros. 70 (8) (2019) 1486–1506.